A&A 433, 997–1006 (2005)
DOI: 10.1051/0004-6361:20041893


Astronomy & Astrophysics

# Warm gas in the cold diffuse interstellar medium: Spectral signatures in the $H_2$ pure rotational lines⋆,⋆⋆

E. Falgarone[1], L. Verstraete[2], G. Pineau des Forêts[2], and P. Hily-Blant[3]

[1] Laboratoire de Radioastronomie, LERMA, École Normale Supérieure, 24 rue Lhomond, 75231 Paris Cedex 05, France
e-mail: edith@lra.ens.fr
[2] Institut d'Astrophysique Spatiale, Bât. 121, Université de Paris XI, 91405 Orsay Cedex, France
e-mail: Laurent.Verstraete@ias.u-psud.fr
[3] IRAM, 300 rue de la Piscine, 38406 Grenoble, France

Received 25 August 2004 / Accepted 3 December 2004

**Abstract.** We present ISO-SWS observations of five pure rotational lines of $H_2$ along a line of sight through the Galaxy which avoids regions of massive star formation. It samples 30 mag of gas, half of it (i.e. 15 mag) being diffuse gas running from the solar neighbourhood to the molecular ring, up to the far side of the Galaxy. The intensities of the S(1) and S(2) lines are too large relative to S(0) to be produced by UV excitation in the known radiation field of the Galaxy. The excitation of these transitions has to tap a more powerful source of energy. We investigate the possibility that it takes place in a large number of magneto-hydrodynamic (MHD) shocks or coherent small-scale vortices, two processes responsible for the intermittent dissipation of MHD turbulence. These dissipation bursts locally and temporarily heat the diffuse gas to temperatures ($T_k \sim 10^3$ K) well above that of the ambient diffuse gas. We compute the spectroscopic signatures of these processes in the $H_2$ lines. Not only are the computed relative line intensities in good agreement with the observations, but the few percent of warm gas involved is consistent with other independent determinations. We find that the fraction of warm $H_2$ in the diffuse gas (i.e. $H_2$ molecules in $J_u \geq 3$ levels) on that line of sight, $N(H_2{}^*)/A_v \approx 4 \times 10^{17}$ cm$^{-2}$ mag$^{-1}$, is the same as that found from far UV spectroscopy in the direction of nearby stars. It is also the same as that estimated in the solar neighbourhood to reproduce the large observed abundances of molecules like $CH^+$. These results suggest that the existence, within the cold neutral medium (CNM), of a few percent of warm gas, for which UV photons cannot be the sole heating source, is ubiquitous and presumably traces the intermittent dissipation of MHD turbulence in the cold diffuse gas.

**Key words.** turbulence – ISM: molecules – ISM: general – infrared: ISM – ISM: evolution – Galaxy: general

## 1. Introduction

The bulk of the mass of the diffuse interstellar medium is in its cold phase, the cold neutral medium (CNM) ($n_H \sim 50$ cm$^{-3}$ and $T_k \sim 80$ K). The CNM is embedded in the warm neutral (WNM) and ionized (WIM) media of low density ($n_H \sim 0.1$ cm$^{-3}$) with temperatures ranging between a few $10^3$ K and $10^4$ K. The existence of small amounts of warm gas intimately associated with the CNM is however suggested by an increasing body of observational data and modelling efforts (Crane et al. 1997; Gredel 1997; Joulain et al. 1998; Flower & Pineau des Forêts 1998; Lucas & Liszt 1996; Gredel et al. 2002; Neufeld et al. 2002).

The earliest manifestations of the existence of such a warm component date back to the discovery in the diffuse medium of large abundances of molecules unable to form at the low temperature and density of the medium. The first to raise this problem was $CH^+$, the formation of which has to overcome the endothermicity $\Delta E/k = 4640$ K of the $C^+ + H_2$ reaction. More recently, a survey of molecular line absorption in the direction of extragalactic continuum sources (see references in Liszt & Lucas 2000) has revealed large abundances of OH and $HCO^+$, a daughter molecule of $CH^+$ in warm chemistry since it is produced via $CH_3^+ + O$ (and $CH_3^+$ is produced by the reactions of $CH^+$ and $CH_2^+$ with $H_2$). This set of lines of sight toward extragalactic sources provides a random sampling of interstellar galactic gas, mostly not associated with molecular clouds. One of the most unexpected results of this survey is the linear correlation between the column densities of $HCO^+$ and OH, observed over a significant dynamical range and the similarity of their linewidths. These two species form via very different chemical patterns but, in poorly shielded environments, they share the need for suprathermal energy to form, the former

⋆ Appendix is only available in electronic form at http://www.edpsciences.org

⋆⋆ Based on observations with ISO, an ESA project with instruments funded by ESA Member States (especially the PI countries: France, Germany, The Netherlands and the UK) and with the participation of ISAS and NASA.

because of the abovementioned endothermicity of the $C^+ + H_2$ reaction and the latter because the $O + H_2$ reaction has an activation energy of $\Delta E/k = 2980$ K.

These molecules are unambiguously ascribed to the CNM because of their narrow line widths (Crane et al. 1995; Liszt & Lucas 2000), and the pivotal role of $H_2$ in the chemistry leading to their formation.

Several models have been proposed to reproduce these large molecular abundances in the diffuse medium. Some invoke supra-thermal velocities of ions relative to the neutrals driven either by Alfvén waves (Federman et al. 1995) or by magneto-hydrodynamic (MHD) shocks (Flower & Pineau des Forêts 1998, and references therein). Another invokes the intermittency of turbulence and the existence of localized tiny warm regions, transiently heated by bursts of ion-neutral friction and viscous dissipation in coherent and intense small scale vortices (Joulain et al. 1998).

Because they concentrate the dissipation of the gas kinetic energy over small sizescales, MHD shocks and coherent vortices in turbulence are the most successful at reproducing the OH versus $HCO^+$ correlation (Flower & Pineau des Forêts 1998; Joulain et al. 1998). Both processes locally heat the neutrals to temperatures in excess of $10^3$ K over timescales long enough to trigger a *hot* chemistry within the cold medium. This heating occurs by ion-neutral drift in the magnetic precursor for the MHD shocks and in the azimuthal streaming of the neutrals relative to the ions in the vortices. In this latter case, another heating mechanism is the viscous dissipation in the layers of strong velocity shear at the outer boundaries of the vortices.

The main differences between MHD shocks and dissipative vortices are their thickness and crossing time. In MHD shocks which have reached a steady-state, the warm layers have a thickness $\approx$0.1 pc and the time for a fluid particle to cross these layers is $\approx 10^4$ yr. By contrast, coherent vortices threaded by magnetic fields, as modelled by Joulain et al. (1998), may be much smaller structures. Radii as small as $\approx$20 AU have been adopted in the present models, resulting from the balance between the stretching action of the large scales of turbulence and the diffusion of the vorticity (i.e. Burgers vortex). The column densities of $CH^+$, OH and $HCO^+$ formed in a single shock or in a single vortex therefore scale as the thickness of the layer of warm gas in each kind of structure i.e. $\approx$a factor $10^3$, and so does the number of such structures required on a line of sight to reproduce the observed amounts of these molecules. The timescale for a fluid particle to cross the warm layers of the vortices is much shorter than for MHD shocks, a few 100 yr only in the case of the thinnest vortices.

The characteristics of the hot chemistry triggered in the shocks and vortices demonstrates that it is not possible, solely on the basis of the abundances they produce, to distinguish between a few MHD shocks or a much larger number of small vortices distributed within the CNM. Pety & Falgarone (2000) have analyzed the spatial and kinematic properties of the regions of largest negative divergence (i.e. shocks) and those of largest vorticity in turbulence (i.e. coherent vortices), and they find, at least in hydrodynamical turbulence, that the two subsets fulfill the observational constraints equally well (surface filling factor, velocity distribution). Whether the chemically active structures in the diffuse medium are shocks or vortices has yet to be established. Although they are dynamically related since shock interactions or curved shocks generate vorticity, a key question is the ultimate scale down to which the turbulent energy of the interstellar medium is cascading. Elongated structures of large velocity shears, possible tracers of the locations of enhanced dissipation of turbulence in translucent molecular clouds, have been observed with variable thickness ranging between 0.02 pc and 0.08 pc (Pety & Falgarone 2003).

The observations reported here directly probe the existence of warm $H_2$ and determine its amount in the cold diffuse medium. Section 2 is devoted to the observations of the pure $H_2$ rotational lines obtained with the ISO-SWS instrument. Section 3 presents the model of the line of sight. In Sect. 4, we show that the observed emission cannot be reproduced with PDR-type emission only and we compare the excess in the S(1) and S(2) lines with the emission of ensembles of low velocity MHD shocks and magnetized vortices. The discussion in Sect. 5 compares the present results, in particular the fraction of warm $H_2$ on that line of sight, with those derived from other data sets.

## 2. ISO-SWS observations of the diffuse galactic medium

### 2.1. Characteristics of the selected line of sight

To trace the presence of warm gas in the cold interstellar medium, we have searched for $H_2$ rotational lines on a long line of sight across the Galactic plane, avoiding as much as possible star-forming regions and giant molecular clouds, to minimize the contribution of bright photo-dissociation regions (PDRs) to the observed $H_2$ lines.

The selected target is a line of sight towards the inner Galaxy, tangent to the molecular ring ($l_{\rm II} = 26.46°$, $b_{\rm II} = 0.09°$). This line of sight is characterized by local minima of the 5 GHz continuum emission (Altenhoff et al. 1970), of the $^{12}$CO line emission (Sanders et al. 1986; Dame et al. 2001) and of the $I(100\,\mu{\rm m})$ emission (Beichman et al. 1988). It therefore avoids bright star forming regions.

The longitude profile of the 100 $\mu$m emission of the inner Galaxy as seen by IRAS and COBE is a superposition of bright discrete sources, associated with giant molecular complexes, and an intense ridge, extending over $\pm 100°$ on either side of the Galactic center (Pérault 1987; Sodrovski et al. 1987, 1989, 1994). On the basis of this longitudinal dependence, the 100 $\mu$m emission at $l_{\rm II} = 26.46°$, $I(100\,\mu{\rm m}) = 1850\,{\rm MJy\,sr^{-1}}$ (Beichman et al. 1988), has been decomposed into 1550 $\rm MJy\,sr^{-1}$ ascribed to the diffuse component and 300 $\rm MJy\,sr^{-1}$ ascribed to molecular clouds.

For simplicity, the line of sight is divided into three domains, one close to the solar circle (i.e. all the gas between 6 and 8 kpc from the galactic center, in the solar neighbourhood and beyond the far side of the molecular ring), a long pathlength tangent to the molecular ring, and the far side of the Galaxy i.e. beyond the solar circle. Their galactocentric distances and velocities derived from the galactic rotation curve of Kerr (1962) are given in Table 1. The HI profile covers the

**Table 1.** Kinematic properties of the three regions sampled by the line of sight and column densities of atomic and molecular hydrogen in dense gas derived from HI and $^{12}$CO(1–0) line profiles.

| | Solar Circle | Molecular Ring | Far side |
|---|---|---|---|
| $R_{GC}$ (kpc) | 6–8 | 4–6 | >8 |
| $v_{lsr}$ (km s$^{-1}$) | 0–40 | 40–130 | 0––50 |
| $W$(HI) ( K km s$^{-1}$) | 2400 | 4000 | 1250 |
| $N$(HI)( cm$^{-2}$) | $4.3 \times 10^{21}$ | $7.2 \times 10^{21}$ | $2.2 \times 10^{21}$ |
| $W$(CO) ( K km s$^{-1}$) | 20 | 40 | – |
| $N(H_2)_{CO}$( cm$^{-2}$) | $5. \times 10^{21}$ | $1. \times 10^{22}$ | – |

velocity range $-50 < v_{lsr} < 130$ km s$^{-1}$ with a half-power width $\Delta v = 130$ km s$^{-1}$ (Weaver & Williams 1973). The CNM sampled by the line of sight therefore runs at all galactocentric radii up to 14 kpc on the far side. By contrast, the $^{12}$CO(1–0) emission is only detected at positive velocities. The column densities of atomic hydrogen and dense molecular hydrogen are derived from the line profiles in each region according to $N(\mathrm{HI}) = 1.8 \times 10^{18}\,\mathrm{cm}^{-2}\ W(\mathrm{HI})$ and $N(H_2)_{CO} = 2.5 \times 10^{20}\,\mathrm{cm}^{-2}\ W(\mathrm{CO})$ (Dame et al. 2001). As expected, more than half of the atomic and dense molecular hydrogen lies in the molecular ring.

The weak free-free emission $T_{cont}(5\ \mathrm{GHz}) = 0.5$ K arises in the ensemble of extended low density (ELD) HII regions of the Galaxy (Mezger 1978). The column density of ionized gas derived from the 5GHz temperature, $N(H^+) = 1.2 \times 10^{21}$ cm$^{-2}$, is low compared to all others.

The total column density of gas on this line of sight is still larger than the sum of all the above. The missing part, i.e. $H_2$ in diffuse gas (i.e. too diluted to excite the $^{12}$CO(1–0) transition), is derived from the $I(100\ \mu\mathrm{m})$ emission and requires a model of the distribution of the dust far-infrared (FIR) luminosity per H mass, $L_{IR}^{H}$, in the Galaxy. It will be discussed in Sect. 3.

### 2.2. ISO-SWS observations and data reduction

The $H_2$ spectra have been obtained with the Short Wavelength Spectrometer (SWS, de Graauw et al. 1996) aboard the Infrared Space Observatory (ISO, Kessler et al. 1996). We performed deep grating line profile scans dedicated to the detection of $H_2$ rotational lines in the ground state.

All the $H_2$ lines, but the S(0) line, are SWS-AOT2 spectra (resolving power $R = \lambda/\Delta\lambda \approx 1500$ to 2000, see Valentijn et al. 1996) taken during revolution 478 (March 8, 1997) of the satellite. Each individual line was observed with a succession of 200 s scans (17.02 $\mu$m-S(1) and 12.23 $\mu$m-S(2) lines: 9 scans each; 9.66 $\mu$m-S(3) and 8.02 $\mu$m-S(4) lines: 5 scans each). For the 28.22 $\mu$m-S(0) line we used a SWS-AOT1 spectrum ($R \approx 600$) taken during revolution 516 (April 15, 1997).

Data reduction was performed within the SWS Interactive Analysis (SWS-IA) environment currently running at the Institut d'Astrophysique Spatiale. The SWS data has a high degree of redundancy. A given resolution element is seen by 12 independent detectors and each scan is repeated twice: a first scan is done with decreasing wavelength (the DOWN scan) then another scan follows with increasing wavelength (the UP scan). Moreover, SWS-AOT2 data is oversampled by a factor of 4 to 5: we thus have 110 integration points per scan (see de Graauw et al. 1996). In addition to standard pipeline reduction procedures, in-house tools were used to obtain the best signal-to-noise ratio because these lines are among the weakest ever detected by ISO-SWS. We detail the reduction steps in the Appendix.

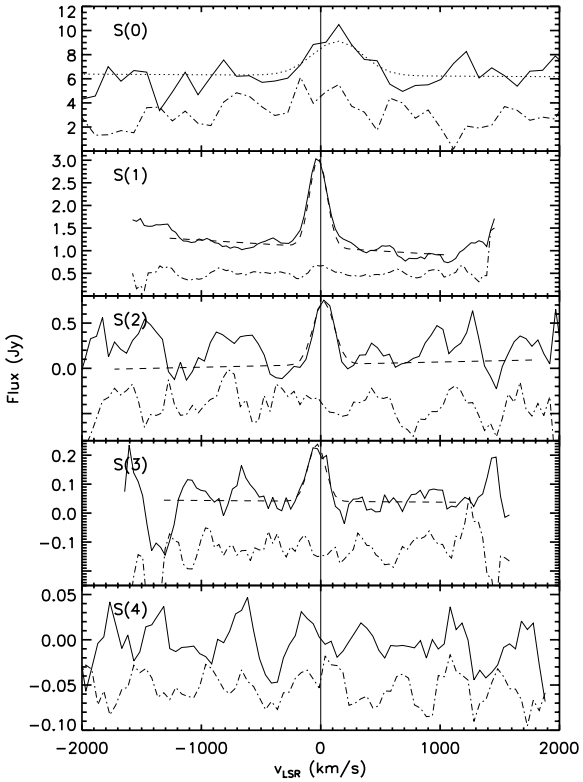


**Fig. 1.** The $H_2$ rotational line profiles observed with SWS (solid line). The dot-dashed line represents the quantity (UP – DOWN)/2 (offset by an arbitrary constant). The dashed line shows the Gaussian fit used to derive the line fluxes given in Table 2. Note that the noise level increases at both ends of the spectra because of poorer redundancy in these spectral ranges (See Appendix).

The spectra are shown in Fig. 1. In all cases, in the central part of the spectra where the instrumental noise is reduced because of a larger redundancy, the UP and DOWN scans are very similar, supporting the fact that the detected lines are not due to transient artefacts. The S(4) line has not been detected and the upper limit to the line flux given in Table 2 ($3\sigma = 0.06$ Jy) is estimated from the rms noise level in the central part of the spectrum (0.02 Jy).

### 2.3. Line fluxes and linewidths

The line fluxes are derived from fits to the line profiles including a Gaussian and an underlying linear continuum (see Fig. 1). Then the integrated line profiles are divided by the beamsizes given in Table 2. We assumed that the source is extended for all $H_2$ lines as suggested by the linewidths (see Table 2) and took the beam profile calibration of Salama (2000). The largest

**Table 2.** Line fluxes and widths of the $H_2$ pure rotational lines. The populations of $H_2$ in each upper level, $N_u$ are derived under the assumption that the lines are optically thin.

| Transition | S(0) | S(1) | S(2) | S(3) | S(4) |
|---|---|---|---|---|---|
| $\lambda(\mu m)$ | 28.2188 | 17.0348 | 12.2786 | 9.6649 | 8.0250 |
| $A_{ul}$ ($s^{-1}$) | $2.94 \times 10^{-11}$ | $4.76 \times 10^{-10}$ | $2.76 \times 10^{-9}$ | $9.84 \times 10^{-9}$ | $2.64 \times 10^{-8}$ |
| $E_u$ (K) | 510 | 1020 | 1700 | 2540 | 3528 |
| $\Omega$ (sr) | $1.6 \times 10^{-8}$ | $9.5 \times 10^{-9}$ | $9.3 \times 10^{-9}$ | $8.6 \times 10^{-9}$ | $8.6 \times 10^{-9}$ |
| $I$ ( erg $s^{-1}$ $cm^{-2}$ $sr^{-1}$) | $3.4 \times 10^{-5}$ | $2.2 \times 10^{-5}$ | $1.3 \times 10^{-5}$ | $4.3 \times 10^{-6}$ | $\leq 1.6 \times 10^{-6}$ |
| *FWHM* (km $s^{-1}$) | 495 | 170 | 203 | 170 | – |
| Resolution (km $s^{-1}$)[1] | 380–475 | 119–156 | 175–226 | 120–150 | 156–192 |
| Source linewidth (km $s^{-1}$)[2] | 139 ± 160 | 67 ± 50 | <160 | 80 ± 50 | |
| $\sigma_{cal}(\%)$[3] | 10 | 10 | 5 | 6 | – |
| $\sigma_{tot}$( erg $s^{-1}$ $cm^{-2}$ $sr^{-1}$)[4] | $1.8 \times 10^{-5}$ | $3.0 \times 10^{-6}$ | $8.0 \times 10^{-6}$ | $2.5 \times 10^{-6}$ | $5.6 \times 10^{-7}$ |
| $\beta$ | 0.98 | 0.95 | 0.85 | 0.72 | 0.94 |
| $I_{corr}$( erg $s^{-1}$ $cm^{-2}$ $sr^{-1}$) | $3.5 \times 10^{-5}$ | $2.3 \times 10^{-5}$ | $1.5 \times 10^{-5}$ | $6.0 \times 10^{-6}$ | $\leq 1.7 \times 10^{-6}$ |
| $N_u$ ($cm^{-2}$) | $2.1 \times 10^{20}$ | $5.3 \times 10^{18}$ | $4.2 \times 10^{17}$ | $3.8 \times 10^{16}$ | $\leq 3.4 \times 10^{15}$ |

[1] Instrumental resolution of the SWS in km $s^{-1}$. The first value is for a point source (de Graauw et al. 1996) and the second value is for an extended source (Salama 2000). Note that the widths of the $H_2$ lines are all close, within the error bars, to the extended source resolution, which indicates that the source is extended.
[2] Source linewidth obtained by deconvolution from the resolution for an extended source. The uncertainty is in the range 50–100 km $s^{-1}$ depending on the wavelength (about one third of the resolution).
[3] Photometric calibration error of the SWS (Leech et al. 2000).
[4] Total rms noise level, (see text).

contribution to the uncertainties given in Table 2 comes from the dispersion found on the line intensities as different data reduction procedures were used.

The detected lines are all marginally resolved. The uncertainties on the measured linewidths given in Table 2 are of the order of one third of the resolution element for the weak lines (in the range 50–100 km $s^{-1}$ depending on the wavelength). The uncertainties on the $H_2$ line central velocities are of the same order of magnitude. In comparison, the $^{12}$CO(1–0) (Cohen et al. 1986) and HI lines (Weaver & Williams 1973) have multiple peaks, half-power widths $\Delta v$ = 80 and 130 km $s^{-1}$ respectively, and line centroid velocities 70 and 40 km $s^{-1}$ respectively. The widths derived for the $H_2$ lines make them more likely to be ascribed to the medium emitting the HI line than the cold dense gas responsible for the $^{12}$CO emission. However, the low spectral resolution precludes any more definite statement. In the following, we assume that the observed $sH_2$ lines arise in the diffuse gas, not in the cold dense gas seen in $^{12}$CO(1–0).

Extinction effects are non-negligible. According to the infrared extinction law of Draine & Lee (1989) and Li & Draine (2001), we find an opacity $\tau$ = 0.7 at 9.66 $\mu$m for the entire line of sight across the diffuse medium ($A_v$ = 15 mag, see Sect. 3). This opacity is due to the strong absorption in the silicate stretch mode. To correct the line intensities for extinction, we have simply assumed that the source of the line emission and the dust absorption are uniformly distributed and mixed along the line of sight. In that case, it is straightforward to show that the emergent intensity is reduced by the factor $\beta = (1 - e^{-\tau})/\tau$ as a function of the integrated opacity, $\tau$. The $\beta$-values are given in Table 2 as well as the line intensities corrected for the extinction, $I_{corr}$. In all the following, we will only deal with observed line fluxes corrected for extinction.

### 2.4. $H_2$ rotational excitation

The intensity $I_{ul}$ of a transition between two levels $u$ and $l$ can be converted into the population $N_u$ of the upper level, under the assumption that the line is optically thin so that $I_{ul} = N_u A_{ul} h\nu/4\pi$. The level populations $N_u$ given in Table 2 for each transition have been derived from the observed line intensities, corrected for extinction $I_{corr}$. We show the excitation diagram in Fig. 2. The relative populations of the $J_u$ = 3 and 5 levels provide a rotational excitation temperature, $T_{rot}$ = 276 K derived from $N(v, J) = g_J g_S e^{-E(v,J)/kT_{rot}}$ where $g_J = (2J + 1)$ is the rotational degeneracy of level $J$ and $g_S = 2I + 1$ is the nuclear spin degeneracy with $I = 0$ for the para lines and $I = 1$ for the ortho lines. It is not a gas kinetic temperature since the densities in the diffuse medium are not high enough, even at $T_k = 10^3$ K, to thermalize the levels above $J_u = 1$ (Le Bourlot et al. 1999).

The column density of excited $H_2$, obtained by summing the populations in the 3 excited levels $J_u = 3, 4$ and 5 is equal to $N^*_{H_2} = 5.8 \times 10^{18}$ $cm^{-2}$ (see Table 2). The question we address in the following section is that of the consistency of this large amount of excited $H_2$ with UV fluorescent excitation in the different regions sampled by the line of sight.

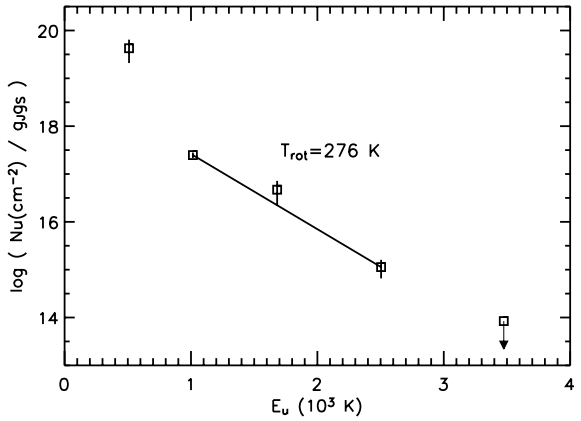


**Fig. 2.** The excitation diagram of the diffuse $H_2$ rotational lines characterized in Table 2. The ordinate represents the column density of the upper level $N_u$ divided by the total degeneracy $g_J\, g_S$ (see text). We assumed an ortho-to-para ratio of 3, i.e. $g_S = 3$. The error bars have been estimated from $\sigma_{\rm tot}$ (see Table 2). The energy of the upper level of the transition $E_u$ is given as abscissa in units of $10^3$ K. The line shows the linear fit between the $J = 3$ and 5 upper levels used to determine the rotational temperature, $T_{\rm rot} = 276$ K.

## 3. Model of the line of sight

Molecular hydrogen is present in the dense molecular clouds traced by the $^{12}$CO(1–0) line but also in the diffuse gas contributing to the HI line profile. In the following, the respective $H_2$ column densities are called $N(H_2)_{\rm CO}$ and $N(H_2)_{\rm diff}$. Their UV excitation and therefore their PDR-type emission depends on their location in the Galaxy. Below, we compute which fraction of $N(H_2)_{\rm diff}$ lies in each environment (solar circle, molecular ring and far side, see Sect. 2.1), diffuse $H_2$ being the amount of gas, in addition to atomic hydrogen, required to explain the $I(100\,\mu{\rm m})$ emission.

The total column density of H nuclei in the diffuse component $N({\rm H})_{\rm diff} = N({\rm HI}) + 2N(H_2)_{\rm diff} + N(H^+)$ is derived from the 100 $\mu$m emission ascribed to the diffuse component (see Sect. 2.1) under the assumption that the dust is heated by the ambient interstellar radiation field (ISRF) at the corresponding galactocentric distance $R_{\rm GC}$.

We neglect the contribution to $I(100\ \mu{\rm m})$ arising in the far side of the Galaxy, these remote regions, unseen in $^{12}$CO, presumably having a very low star formation rate and accordingly a low UV flux. We also neglect the FIR emission arising in the ELD because the overall column density is small, in comparison to that of the neutral gas. The diffuse $I(100\ \mu{\rm m})$ emission therefore originates only in the neighbourhood of the solar circle and in the molecular ring, from dust column densities in proportion to those of HI (resp. 37% for the solar circle and 63% for the molecular ring, see Table 1). The values of $L^{\rm H}_{\rm IR}$, the FIR luminosity per H mass, adopted for the diffuse contribution of each region ($L^{\rm H}_{\rm IR}(SC)$ for the solar circle and $L^{\rm H}_{\rm IR}(MR)$ for the molecular ring, see Table 3) are averages over the relevant galactocentric distances of the radial profile found by Pérault (1987) in his model of the FIR galactic emission. Expressing the contribution of each region to the 100 $\mu$m emission:

$$4\pi\nu I(100\,\mu{\rm m}) = \mu_{\rm H}[\,0.37\,L^{\rm H}_{\rm IR}(SC) + 0.63\,L^{\rm H}_{\rm IR}(MR)\,]N({\rm H})_{\rm diff}$$

(where $\mu_{\rm H}$ is the mean mass per proton) provides $N({\rm H})_{\rm diff} = 2.7\times10^{22}$ cm$^{-2}$ or 15 magnitudes of diffuse gas, from which we derive the $H_2$ column densities present in each diffuse component (Table 3), by simply subtracting the corresponding value of $N$(HI) (Table 1). The total $H_2$ column density present in the diffuse component is thus $N(H_2)_{\rm diff} = 8\times10^{21}$ cm$^{-2}$. Note that the average fractional abundance of H nuclei in the form of $H_2$ in the diffuse component, $f = 2\,N(H_2)_{\rm diff}/N({\rm H})_{\rm diff} = 0.6$ is within the range found by the Copernicus data in the solar neighbourhood (Savage et al. 1997).

The description of the material distributed along this line of sight is coarse, but its consistency is provided by the fact that the $H_2$ column density in the GMC component of the molecular ring is about the same when derived from either the CO line (Table 1) or the FIR emission, $I(100\,\mu{\rm m}) = 300$ MJy sr$^{-1}$ with the appropriate low $L^{\rm H}_{\rm IR}$ ascribed to this well-shielded component (Table 3). The uncertainty on the $H_2$ column density present in the diffuse component is mostly due to the use of the exponential decay of the FIR luminosity per H nucleus with galactocentric distance because it involves an axisymmetric representation of the Galaxy. The average FIR luminosity per H mass in the HI, $L^{\rm H}_{\rm IR} = 5\ L_\odot/M_\odot$, found by Sodrovski et al. (1994) for this range of longitude is only 25% smaller than what we use, taking into account the mass fraction in each radiative environment along this line of sight. We thus estimate that we may have underestimated the column density of diffuse gas along that line of sight by 25%. As an illustration, by using an average value $L^{\rm H}_{\rm IR} = 5.4\ L_\odot/M_\odot$ over all galactocentric distances, we find $N(H_2)_{\rm diff} = 10^{22}$ cm$^{-2}$.

In the direction of the molecular ring, the stellar Lyman continuum flux responsible for the ionization of the ELD HII regions is about 8 times larger than that in the solar neighbourhood (Güsten & Mezger 1983; Puget 1985; Pérault 1987). Photodissociation regions (PDRs) illuminated by the UV radiation field in the molecular ring are therefore expected to develop at the edges of molecular clouds. We infer the existence of such PDRs on the line of sight, characterized by $G_0 \approx 10$, $G_0$ being the UV flux in units of the Habing field ($I_{\rm UV} = 1.6\times10^{-3}$ erg cm$^{-2}$ s$^{-1}$). In contrast, Wolfire et al. (2003) find that the midplane FUV intensity in the inner Galaxy is only 3 times larger than in the solar neighbourhood. Consequently, an upper limit of the PDR-type emission of cloud edges irradiated by the UV field in the molecular ring is obtained by adopting $G_0 = 10$. This is used in Sect. 4 to provide an upper limit of the PDRs contribution to the observed $H_2$ lines.

In summary, the selected line of sight samples about (i) 6 mag of diffuse gas in the ISRF of the solar circle neighbourhood ($G_0 = 1$); (ii) 9 mag of diffuse gas in the ISRF of the molecular ring ($G_0 \le 10$); and (iii) 15 mag of dense gas in the molecular ring ($G_0 \le 10$). $H_2$ molecules are present in all these three components, thus each of them contributes to the $H_2$ line emission. In the next section, we show that their PDR-type emission cannot account for the observed S(1) and S(2) line intensities.

**Table 3.** Total gas column densities derived from the far infra-red emission. Both the solar circle and the molecular ring contribute to the diffuse emission.

| | Diffuse emission | | GMCs emission |
|---|---|---|---|
| $I(100\,\mu m)$ (MJy sr$^{-1}$) | 1550 | | 300 |
| | Solar circle (SC) | Molecular ring (MR) | GMCs (MR) |
| $L_{IR}^{H}$ ($L_\odot/M_\odot$) | 2.0 | 9.5 | 1.2 |
| $N(H)_{diff}$ (cm$^{-2}$) | $1.0\times10^{22}$ | $1.7\times10^{22}$ | |
| $N(H)_{CO}$ (cm$^{-2}$) | – | – | $2.7\times10^{22}$ |
| $N(H_2)_{diff}$ (cm$^{-2}$) | $3\times10^{21}$ | $5\times10^{21}$ | |
| $N(H_2)_{CO}$ (cm$^{-2}$) | – | – | $1.35\times10^{22}$ |

## 4. Comparison of observations with model predictions

### 4.1. PDR-type emission: Fluorescent excitation

Both the ensemble of diffuse clouds building up the 15 mag of diffuse gas sampled by the line of sight and the dense molecular clouds traced by $^{12}$CO(1–0) have edges irradiated by UV photons which contribute to the $H_2$ PDR-type emission of this line of sight. The $H_2$ line intensities are computed in the framework of the PDR model of Le Bourlot et al. (1993) which has been considerably updated since then (Le Petit et al. in preparation)[1]. It includes 113 chemical species and 967 chemical reactions. The 250 first levels of $H_2$ are considered. The UV line opacity and self-shielding of all individual lines contributing to the UV pumping are computed at each depth in the cloud, so that the effects induced by the different opacities of the ortho and para pumping lines discussed in Sternberg & Neufeld (1999) are properly taken into account. The opacity of the lines responsible for the radiative cooling is also taken into account. The adopted gas phase abundances are $[C] = 1.38\times10^{-4}$ and $[O] = 3.00\times10^{-4}$, representative of the cold, diffuse interstellar medium in the solar neighbourhood (Savage & Sembach 1996) and only 20% larger in the molecular ring (Giveon et al. 2002). The ionisation rate by cosmic rays is $\zeta = 5\times10^{-17}$ s$^{-1}$. The model solves the equations of thermal and chemical balance as a function of depth in the cloud in a plane-parallel geometry. The density is assumed uniform, and the UV illumination is either one-side or two-side, depending on the model computed.

As discussed above, estimating the PDRs contribution to the observed $H_2$ spectrum on this line of sight involves the UV field in each galactic region but also the fragmentation of the gas, the number of irradiated edges intercepted by the line of sight increasing with the level of fragmentation.

There is no source possibly associated with star forming regions on the line of sight. We therefore adopt $G_0 = 10$ in the molecular ring to compute an upper limit to the PDR-type emission (see Sect. 2.1). This parameter is also constrained by the fine structure lines observed along the same line of sight by the ISO-LWS (Caux et al., in preparation). The observed ratio [OI 63 $\mu$m]/[CII 158 $\mu$m] $\sim$ 0.12 is small, which precludes the existence on the line of sight of PDRs with $G_0 > 10$ (Kaufman et al. 1999), unless a [O]/[C] ratio much smaller than that used in the model is relevant.

The fragmentation of the diffuse gas into small clouds must be consistent with the average $H_2$ fraction $N(H_2)_{diff}/N(H)_{diff} = 0.3$. In the solar neigborhood ($G_0 = 1$), this imposes that individual clouds have column densities of at least $N_H = 6\times10^{20}$ cm$^{-2}$ for $n = 30$ cm$^{-3}$ ($\delta A_v = 0.3$ mag), while in the molecular ring with $G_0 = 10$, the lower limit is $N_H = 3\times10^{21}$ cm$^{-2}$, for $n = 100$ cm$^{-3}$. The constraint for the dense PDRs (edges of clouds detected in the CO line) is provided by the existence of CO: dense gas cannot be subdivided into structures more transparent than 2 magnitudes for $G_0 = 10$, otherwise CO would be photodissociated. Illustration of the effects of fragmentation are given in Fig. 3. The S(1)/S(0) line ratio is the most affected because fragmentation increases the heating rate, thus the gas temperature. However, the overall emission is not much increased because $H_2$ is more photodissociated. The last constraint is obviously that the total column density $N(H)$ does not exceed that derived from $I(100\,\mu m)$. The maximum number of clouds of each kind, $N_c$, consistent with these constraints is given in Table 4 for the diffuse and dense components.

Figure 3 displays an ensemble of individual PDR models intended to illustrate the influence of the radiation field, of the metallicity and fragmentation of the gas. The main feature, relevant for these low excitation PDRs, is that the S(2)/S(3) and S(3)/S(4) line ratios are barely sensitive to any of these parameters because the upper levels of each of these transitions are populated by fluorescence only. The level of fragmentation has no impact on these line ratios for instance. At the opposite, the S(0)/S(1) and S(1)/S(2) are sensitive to model parameters because the levels $J_u = 2$ and 3 are mostly collisionally excited and their population depends on the gas temperature.

We have computed an upper limit of the spectrum of the PDR-type emission of the whole line of sight according to the model described above. The resulting spectrum displayed in Fig. 3 (left) corresponds to the cumulated emission of (i) 19 diffuse PDRs of thickness $\delta A_v = 0.3$ mag illuminated on both sides by the UV field at the solar circle, plus that of (ii) 5 diffuse PDRs of thickness $\delta A_v = 2$ mag and (iii) 7.5 dense PDRs illuminated on two sides by the UV field of the molecular ring. The latter are the main contributors to the S(2), S(3) and S(4) lines. Finally, the line intensities have been multiplied

[1] The updated version of the PDR code is available at the address: `http://aristote.biophys.jussieu.fr/MIS`

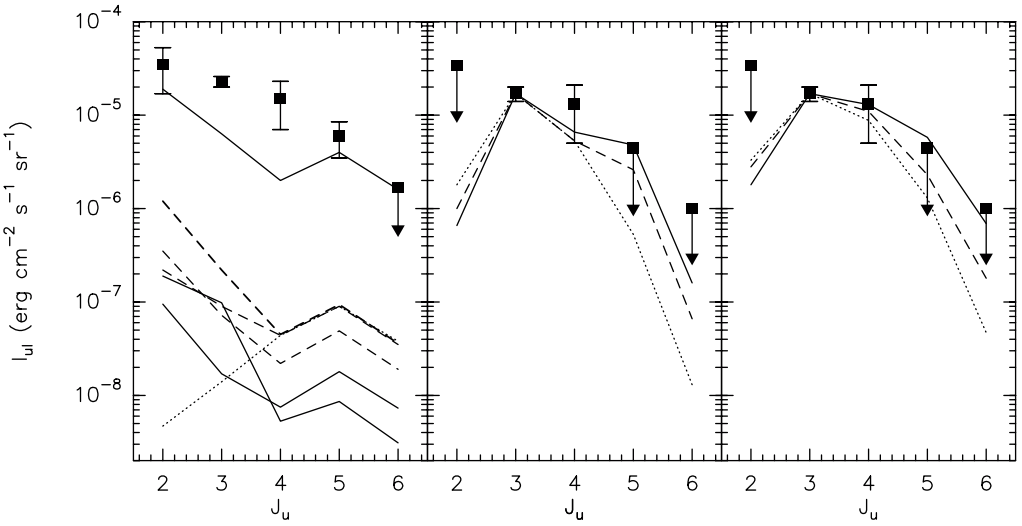


**Fig. 3.** *Left*: observed $H_2$ line intensities corrected for extinction (solid squares) and PDR model predictions. The bottom spectra are from individual PDRs: (i) diffuse PDRs in the radiative environment of the solar circle, $G_0 = 1$ (solid) with one-side illumination (thin) or two-side illumination (thick) of a cloud of thickness $\delta A_v = 0.3$ mag and density $n_H = 30$ cm$^{-3}$; (ii) diffuse PDRs in the molecular ring radiative environment ($G_0 = 10$) at the edge of a cloud of thickness $\delta A_v = 2$ mag and $n_H = 100$ cm$^{-3}$: solar metal abundances with one-side illumination (thin dashed) or two-side illumination with solar (thick dashed) or twice solar (medium dashed) metal abundances; (iii) dense PDRs in the molecular ring, $n_H = 10^4$ cm$^{-3}$ (dotted). The upper spectrum is the PDR-type emission of the entire line of sight, as modelled (see text). *Center*: residual emission (i.e. observed emission – modelled PDR-type emission) (solid squares). Model predictions of 49, 21 and 12 MHD shocks travelling at 8 (dotted), 10 (dashed) and 12 km s$^{-1}$ (full) respectively in gas of density $n_H = 50$ cm$^{-3}$ with $B = 7$ $\mu$G (see text for details). *Right*: residual emission and model predictions of a large number of magnetized vortices in gas of density $n_H = 30$ cm$^{-3}$ with $B = 10$ $\mu$G. The dashed and full lines are for $10^4$ and $1.2 \times 10^4$ vortices of rotational velocity $v_D = 3.5$ and 4 km s$^{-1}$ respectively. The lowest spectrum (dotted) corresponds to the case $v_D = 3.5$ km s$^{-1}$ for which the assumption of statistical equilibrium for the populations of the $H_2$ rotational levels is removed. In these plots, the numbers of shocks and vortices are adjusted so that the S(1) line intensity is that of the residuals.

**Table 4.** Model of the PDR-type emission of the line of sight. $N$(H) and $A_v = N(H)/1.8 \times 10^{21}$ are the total column densities of protons in each component, as derived from $I(100\,\mu m)$ (Table 3). $\delta A_v$ is the lower limit of the thickness of individual clouds illuminated on both sides consistent with the fraction of $H_2$, $N(H_2)/N(H) = 0.3$, derived for the diffuse medium and the presence of CO in the dense gas (see text). Hence, $N_c = A_v/\delta A_v$ is the largest number of clouds of each kind. In each component, the PDR models shown in Fig. 3 are computed for the corresponding values of $G_0$ and total density $n_H$.

| | Diffuse SC 6–8 kpc | Diffuse MR 4–6 kpc | Dense MR |
|---|---|---|---|
| $N$(H) (cm$^{-2}$) | $10^{22}$ | $1.7 \times 10^{22}$ | $2.7 \times 10^{22}$ |
| $A_v$ | 5.6 | 9.4 | 15 |
| $\delta A_v$ | 0.3 | 2 | >2 |
| $N_c$ | 19 | 5 | <7.5 |
| $G_0$ | 1 | 10 | 10 |
| $n_H$ (cm$^{-3}$) | 30 | 100 | $10^4$ |

by a factor of 2 to take into account a possible inclination of the planar PDRs.

The estimated upper limit of the PDR-type contribution on the line of sight has been removed from the observed spectrum (corrected for extinction). The residual $H_2$ line intensities are shown in the central and right panels of Fig. 3 with the observed error bars. Although the estimated PDR-type emission of the line of sight is model-dependent, the residual S(2) line intensity is constrained by the observational upper limit on S(4), since the S(2)/S(3) and S(3)/S(4) line ratios are only weakly sensitive to model parameters. We discuss below a possible source for this residual line emission.

### 4.2. Contribution from collisionally excited $H_2$ in warm gas

Figure 3 clearly shows that the S(1) and S(2) $H_2$ line intensities detected by ISO-SWS are too large compared to that of the S(0) line to be PDR-type emission in a low UV environment. Except for the S(0) line, consistent with PDR-type excitation, the observed intensities reveal a non negligible fraction of *warm* $H_2$, too warm to be heated by the known UV field along this line of sight. As discussed in Sect. 1, an alternative source of heating is the intermittent dissipation of interstellar turbulence. We have therefore computed the line emission in the pure rotational lines of MHD shocks and magnetized vortices, taken as templates of the dissipative structures of MHD turbulence and disseminated in the 15 mag of diffuse gas sampled by the line of sight.

For the MHD shocks, the results derived from the model calculations of Flower & Pineau des Forêts (1998) are shown in Fig. 3 for different shock velocities. The MHD shock models have also been updated, in particular with the new cross-sections of collisional excitation of $H_2$ (Le Bourlot et al. 1999; Flower 1998). Shocks are assumed to have reached steady-state. The given numbers of MHD shocks at each velocity

match the intensity of the S(1) line residual. The smaller the shock velocity, the larger the number of shocks required to reproduce the observed intensities. The higher the shock velocity, the larger the power in the S(2) and S(3) lines because the peak temperature of the neutrals increases with the shock velocity (from 800 K for shocks at 8 km s$^{-1}$ to 1300 K for shocks at 12 km s$^{-1}$). For a given shock velocity, the preshock gas density has no influence on the shape of the emergent spectrum, it only affects the number of shocks required to reproduce the observed intensities. The larger the ionisation degree of the preshock gas, the better the coupling of the neutrals to the ions, and the warmer and narrower the shock. Here, we have $n_e/n_H = 1.5 \times 10^{-4}$ in the preshock gas, resulting from UV ionization. All the shocks with velocities $V_s \geq 8$ km s$^{-1}$ are consistent with the observed spectrum.

For the vortices, three predicted spectra are shown in Fig. 3 for about $10^4$ vortices. Again, the numbers of vortices intercepted by the line of sight match the residual intensity of the S(1) line. The model predictions are those of Joulain et al. (1998) in the case of their standard model ($n_H = 30$ cm$^{-3}$, $B = 10$ $\mu$G), and two different values, $v_D = 3.5$ and 4 km s$^{-1}$, of the ion-neutral drift velocity induced by the rotation of the neutrals. The range of drift velocities we consider is narrow because, as explained in Joulain et al. (1998), the ion-neutral drift velocity is that of the neutrals in the vortex and it is constrained by the rms velocity of the ambient turbulence in the CNM. The upper spectra are obtained with assumed statistical balance among the rotational levels. For the lower spectrum ($v_D = 3.5$ km s$^{-1}$), this assumption is removed because of the short time scales involved in the vortex dynamics (a few 100 yr).

The observed S(1) and S(2) residual intensities are therefore reasonably reproduced by either an ensemble of MHD shocks travelling at velocities in the range 8–10 km s$^{-1}$ or a much larger number of small magnetized vortices scattered along the line of sight. The similarity between the shocks and vortex spectra is due to the fact that the $H_2$ peak kinetic temperature reached in these structures are similar. Their differences, i.e. the relative intensity of the ortho and para lines (or the ortho/para ratio), originate in the very different timescales associated with each of them ($\sim 10^4$ yr versus a few 100 yr), given the initial conditions in the preshock gas. It is interesting to note here that the MHD shocks cannot be distinguished from the magnetized vortices by the spectra of their $H_2$ rotational lines.

### 4.3. The fraction of warm gas along the line of sight

We have shown in the previous section that the observed excess of S(1) and S(2) emission above PDR-type emission can be accounted for by a number of warm structures with gas at $T_k \approx 10^3$ K, temporarily heated to that temperature by locally large ion-neutral streaming and viscous dissipation.

It is interesting to compute the fraction of warm $H_2$ within the ambient diffuse medium, at $T_k = 80$ K. We define $N(H_2^*)$ as the column density of $H_2$ molecules in the rotational levels $J_u \geq 3$. The column densities of excited $H_2$ (i.e. $H_2$ in the warm layers) of each type of individual dissipative structure, $N_{sh}(H_2^*)$ and $N_{vor}(H_2^*)$ are given in Table 5. Their number per magnitude of diffuse gas sampled is simply the number required to reproduce the S(1) residual intensity (see caption of Fig. 3) divided by the depth of the line of sight in diffuse gas, i.e. 15 mag. From these values, we infer an average value of the amount of warm $H_2$ per magnitude of gas. They are given in the last column of Table 5.

**Table 5.** Column densities, $N_{sh}(H_2^*)$ and $N_{vor}(H_2^*)$, of $H_2$ molecules in rotational levels $J_u \geq 3$ in the models of single MHD shocks and magnetized vortices discussed in the text. The number of such structures per magnitude of gas sampled, required to reproduce the observed $H_2$ residuals in 15 mag of diffuse gas is given in Col. 4. Note that the column density of excited $H_2$ per magnitude (Col. 5) is of the same order of magnitude in all the cases.

| **MHD** | $V_s$ | $N_{sh}(H_2^*)$ | Number | $N(H_2^*)/A_v$ |
|---|---|---|---|---|
| **shocks** | km s$^{-1}$ | cm$^{-2}$ | per mag | cm$^{-2}$/mag |
| | 8 | $1.5 \times 10^{17}$ | 3.2 | $4.8 \times 10^{17}$ |
| | 10 | $3.5 \times 10^{17}$ | 1.4 | $4.9 \times 10^{17}$ |
| | 12 | $6.2 \times 10^{17}$ | 0.8 | $5.0 \times 10^{17}$ |
| **Vortices** | $v_D$ | $N_{vor}(H_2^*)$ | Number | $N(H_2^*)/A_v$ |
| | km s$^{-1}$ | cm$^{-2}$ | per mag. | cm$^{-2}$/mag |
| | 3.5 | $1.7 \times 10^{14}$ | 666 | $1.1 \times 10^{17}$ |
| | 4 | $3.6 \times 10^{14}$ | 800 | $2.9 \times 10^{17}$ |

On average, the ensembles of shocks correspond to 6% of gas at kinetic temperature ($T_k > 800$ K) along the line of sight. In the case of magnetized vortices, the total number required along the line of sight to reproduce the $H_2$ line intensities is large but corresponds to only 1% of the gas being at $T_k > 10^3$ K. In the above determinations, we have not taken into account the beam dilution of individual structures (shock or vortex) because their surface filling factor, as ensembles, has been estimated to be close to unity, given the large frequency of occurrence of $CH^+$, $HCO^+$ and OH absorption lines observed in the direction of nearby stars and extragalactic radio sources in the diffuse medium (see the discussion in Joulain et al. 1998).

## 5. Discussion

The whole argument presented in this paper is prone to criticism because the $H_2$ lines are among the weakest detected by ISO-SWS and the excess of $H_2$ emission above PDR-type emission relies on our modelling this long line of sight across the Galaxy as well as the PDR model itself. Yet, our interpretation is based on prominent features, namely the fact that the S(1) and S(2) lines are respectively about 4 and 7 times brighter than the modelled PDR-type emission of the whole line of sight. Moreover, the existence of warm $H_2$ associated with colder gas and the need for an alternative source of excitation is corroborated by other data sets.

### 5.1. Warm $H_2$ in external galaxies

Valentijn & van der Werf (2000) have mapped the $H_2$ S(0) and S(1) lines along the galactic disk of the edge-on galaxy NGC 891. They infer the existence of two gas components from the different spatial distributions of the two lines. The warm component is scattered throughout the disk, while the cool component dominates the signal in the outer regions of the galaxy. They acknowledge that excitation conditions derived from the comparison of only the S(0) and S(1) lines may be erroneous, since the two lines may not arise in the same gas component. Interestingly, the S(1) line intensity they measure in the direction of the molecular ring of this spiral galaxy is $1.4 \times 10^{-5}$ erg cm$^{-2}$ s$^{-1}$ sr$^{-1}$, hence of the same order of magnitude as what we measure for the same line, $2.3 \times 10^{-5}$ erg cm$^{-2}$ s$^{-1}$ sr$^{-1}$ (see Table 2) along the line of sight tangent to the molecular ring in our Galaxy. The kinetic temperature they estimate for this warm gas component ($T_k$ = 150–230 K) is also larger than the temperature of the diffuse medium. This suggests that a comparable small fraction of warm $H_2$ may exist in the cold diffuse component of external galaxies similar to the Milky Way, with a surface filling factor of the warm structures close to unity in both cases.

### 5.2. Signatures of warm $H_2$ in the solar neighbourhood

Early far UV absorption studies with the *Copernicus* satellite showed the presence of significant amounts of excited $H_2$ ($N(H_2^*) \sim$ a few $10^{17}$ cm$^{-2}$ mag$^{-1}$) in nearby diffuse clouds (Spitzer et al. 1974; Morton 1975; Snow 1976; Spitzer & Morton 1976; Savage et al. 1977; Frisch 1980). Theoretical modelling of the $H_2$ excitation suggested then that the high-$J$ levels are dominantly populated by collisions in MHD shocks (Draine & Katz 1986; Pineau des Forêts et al. 1986; van Dishoeck & Black 1986).

More recently, new far UV spectra at higher resolution and sensitivity obtained with the Far UV Spectroscopic Explorer (*FUSE*) in the direction of three nearby late-B stars (Gry et al. 2002) also reveal the existence of small amounts of $H_2$ collisionally excited in warm, diffuse gas. The lack of any 100 $\mu$m halo emission centered on these stars supports the fact that they do not heat their surrounding interstellar matter above what the ambient UV field does. Therefore the large column densities inferred for the level populations in the $J_u \geq 3$ levels are neither due to UV fluorescence nor collisional excitation in gas heated by the ambient UV field. They have to be due to collisional excitation in warmer gas.

Quantitatively, the column densities of $H_2$ in the rotational levels $J_u \geq 3$ per magnitude of gas derived from these observations are 5.4, 1.5 and $1.6 \times 10^{17}$ cm$^{-2}$ mag$^{-1}$ for each star respectively. This amount is very close to the average values of warm $H_2$ per magnitude of diffuse gas we give in Table 5. This result strengthens the idea that the fraction of warm gas in the cold diffuse medium is the same at different galactocentric distances and that the processes responsible for the heating of that gas are ubiquitous.

### 5.3. Indirect evidence for warm $H_2$: The $CH^+$ abundance

In the solar neighbourhood, the column density of $CH^+$ approximately increases with the total H column density as $N(CH^+) \approx 6 \times 10^{-9} N(H)$. The linearity of this relation suggests that $A_v$ does not trace an increase of the gas shielding but simply an increase of the number of $CH^+$-emitting regions sampled by the line of sight as the extinction $A_v$ to the star increases i.e. the column density on the line of sight increases. This was already a conclusion reached by Gredel (1997). As the formation of $CH^+$ has to tap a more powerful source of energy than that provided by the ambient UV field, as for instance gas supersonic turbulence, this relation enables an estimate of the number of dissipative structures per magnitude of diffuse gas required to reproduce the observed column densities of $CH^+$.

Gredel et al. (2002) reproduce the observed column densities of $CH^+$ towards a large set of nearby stars by adding an ad hoc component to the diffuse medium, made off a number of low velocity (<10 km s$^{-1}$) criss-crossing MHD shocks. The number of shocks they need vary with the sight lines but the average values are respectively 20 and 5 shocks per magnitude for shock velocities of 8 and 9 km s$^{-1}$ respectively. These numbers are of the same order of magnitude as those we derive from the $H_2^*$ column density (Table 5).

Similarly, each magnetized vortex in the solar neighbourhood conditions and a shielding against the ambient UV field $A_v$ = 0.2 mag, produces a column density $N(CH^+) = 2 \times 10^{10}$ cm$^{-2}$, for a vortex velocity $v_D$ = 3.5 to 4 km s$^{-1}$ (Joulain et al. 1998). The number of such vortices per magnitude of gas sampled, required to reproduce the above correlation between $N(CH^+)$ and $N(H)$ is therefore ≈500, a number to be compared to those given in Table 5.

These comparisons provide orders of magnitude only, since molecular abundances are sensitive to UV shielding, and results established in the solar neighbourhood conditions should not be extrapolated to inner galaxy conditions without caution. Nevertheless, these orders of magnitude are of interest. Since the line of sight of our SWS observations samples gas in the molecular ring and gas in the far side of the Galaxy, our results suggest that the fraction of warm gas in the diffuse component does not vary significantly with galactocentric distance. If the heating source for the warm gas is the dissipation of supersonic turbulence in shocks or vortices (or both), this implies that in denser regions (on average) such as the molecular ring, the dissipation rate is larger, to ensure a similar amount of warm gas. In the case of vortices, the same peak kinetic temperature is obtained in a gas of density $n_H = 100$ cm$^{-3}$ for a dissipation rate of the turbulence only twice as large as in the solar neighbourhood. A higher dissipation rate in the inner Galaxy is expected because the turbulent velocity in the diffuse gas is larger as suggested by the large internal velocity dispersion of molecular clouds in the molecular ring (e.g. Teyssier et al. 2001).

## 6. Conclusion

The S(1) and S(2) $H_2$ rotational lines detected along a long line of sight devoid of active star forming regions, towards the

inner Galaxy, cannot be excited only by UV photons. Their collisional excitation has to be fed by a more powerful source of heating. We have shown that the observed line intensities are consistent with the line emission of a large number of MHD shocks or magnetized coherent vortices scattered along the line of sight, taken as templates for the dissipative processes of MHD turbulence. A remarkably small (a few %) fraction of *warm* gas ($T_k \sim 10^3$ K) on the line of sight is sufficient to reproduce the observed line intensities. In our scenario, the warm gas is heated by ion-neutral drift in the magnetic precursor of the MHD shocks or the azimuthal streaming of the neutrals in the vortices. Viscous dissipation in the layers of large velocity shear at the vortex boundary is also present. These few % of warm gas are distributed among a few MHD shocks per magnitude of diffuse gas, and a much larger ($\sim 10^3$) number of vortices. This is because, as modelled, the MHD shocks in diffuse gas are thicker structures (~0.1 pc) than the vortices (~20 AU).

Interestingly, the column density of excited $H_2$ (computed as the sum of the populations of the levels $J = 3$ to 5) per magnitude of diffuse gas, $N^*_{H_2}/A_v \approx 4 \times 10^{17}\,\mathrm{cm^{-2}\,mag^{-1}}$ is close to the values derived from far UV spectroscopy in the direction of three late B stars of the solar neighbourhood. Moreover, the number density of dissipative structures (per magnitude of gas sampled) required to reproduce the $H_2$ line intensities along this long line of sight is similar to that required in the solar neigborhood to reproduce the observed abundances of $CH^+$. These comparisons suggest that the mechanism responsible for the generation of the warm gas, namely the bursts of dissipation of turbulence, in shocks or in vortices, operates in the inner parts of the Galaxy at a rate such that the fraction of gas at $T_k \sim 10^3$ K is roughly constant. This is also in line with the detection of a similar S(1) $H_2$ line intensity across the molecular ring in the spiral galaxy NGC891.

*Acknowledgements.* We are indebted to J.-L. Puget for inserting this project in his ISO Mission Scientist guaranteed time and for his help in the elaboration of the proposal. We are grateful to Edwin Valentijn for introducing us to powerful data reduction methods. We thank the MPE-SDC (Garching) and the DIDAC (Groningen) for their constant support in the data reduction phase and with the use of SWS-IA3. SWS-IA3 is a joint development of the SWS consortium. Contributing institutes are SRON, MPE, KUL and the ESA Astrophysics division. We thank Dave Hollenbach for his close reading of the manuscrit and his suggestions which helped us improve the paper. We thank the anonymous referee for her/his stimulating criticisms and questions.

## References

Altenhoff, W. J., Downes, D., Goad, L., Maxwell, A., & Rinehart, R. 1970, A&AS, 1, 319
Beichman, C. A., Neugebauer, G., & Habing, H. J. 1988, IRAS Explanatory Supplement
Crane, P., Lambert, D. L., & Sheffer, Y. 1995, ApJS, 99, 107
Dame, T. M., Hartmann, D., & Thaddeus, P. 2001, ApJ, 547, 792
van Dishoeck, E., & Black, J. H. 1986, ApJS, 62, 109
Draine, B. T., & Lee, H. M. 1984, ApJ, 285, 89
Draine, B. T., & Katz, N. 1986, ApJ, 310, 392
Federman, S. R., Rawlings, J. M. C., Taylor, S. D., & Williams, D. A. 1996, MNRAS, 279, 41
Flower, D. R. 1998, MNRAS, 297, 334
Flower, D. R., & Pineau des Forêts, G. 1998, MNRAS, 297, 1182
Frisch, P. C. 1980, ApJ, 241, 697
Giveon, C., Morisset, C., & Sternberg, A. 2002, A&A, 392 501
de Graauw, T., Hasler, L. N., Beintema, D. A., et al. 1996, A&A, 315, L49
de Graauw, T. 2000 The Universe as seen by ISO, ed. P. Cox, & M. F. Kessler, ESA SP-427
Gredel, R. 1997, A&A, 320, 929
Gredel, R., Pineau des Forêts, G., & Federman, S. R. 2002, A&A, 389, 993
Gry, C., Boulanger, F., Nehmé, C., et al. 2002, A&A, 391, 675
Güsten, R., & Mezger, P. 1983, Vistas Astron., 26, 159
Joulain, K., Falgarone, E., Pineau des Forêts, G., & Flower, D. 1998, A&A, 340, 241
Kaufman, M. J., Wolfire, M. G., Hollenbach, D. J., & Luhman, M. L. 1999, ApJ, 527, 795
Kerr, F. J. 1962, MNRAS, 123, 327
Kessler, M. F., Steinz, J. A., Anderegg, M. A., et al. 1996, A&A, 315, L27
Le Bourlot, J. 2000, A&A, 360, 656
Le Bourlot, J., Pineau des Forêts, G., & Flower, D. R. 1999, MNRAS, 305, 802
Leech, K., et al. 1998, SWS Instrument Data User's Manual, Issue 1.0, SAI/2000-008/Dc
Li, A., & Draine, B. T. 2001, ApJ, 550, L213
Liszt, H. S., & Lucas, R. 2000, A&A, 355, 333
Lucas, R., & Liszt, H. S. 1996, A&A, 307, 237
Mezger, P. 1978, A&A, 70, 565
Morton, D. C. 1975, ApJ, 197, 85
Neufeld, D. A., Kaufman, M. J., Goldsmith, P. F., Hollenbach, D. J., & Plume, R. 2002, ApJ, 580, 278
Pérault, M. 1987, Ph.D. dissertation, Université Paris VII
Pety, J., & Falgarone, E. 2000, A&A, 356, 279
Pety, J., & Falgarone, E. 2003, A&A, 412, 417
Pineau des Forêts, G., Flower, D. R., Hartquist, T. W., & Dalgarno, A. 1986, MNRAS, 220, 801
Porter, D. H., Pouquet, A., & Woodward, P. R. 1994, Phys. Fluids, 6, 2133
Puget, J.-L. 1985, in Birth and infancy of stars, Les Houches summer school, ed. A. Omont, & R. Lucas (North Holland Publ.)
Salama, A. 2000, ISO beyond point sources: Studies of extended IR emission, ESA SP-455
Sanders, D. B., Clemens, D. P., Scoville, N. Z., & Solomon, P. M. 1986, ApJS, 60, 1
Savage, B. D., & Sembach, K. R. 1996, ARA&A, 34, 279
Savage, B. D., Drake, J. F., Budich, W., & Bohlin, R. C. 1977, ApJ, 216, 291
Schaiedt, S. G., Morris, P. W., Salama, B., et al. 1996, A&A, 315, L55
Snow, T. P. 1976, ApJ, 204, 759
Sodrovski, T. J., Dwek, E., Hauser, M. G., & Kerr, F. J. 1987, ApJ, 322, 101
Spitzer, L., & Morton, D. C. 1976, ApJ, 204, 731
Spitzer, L., Cochran, W. D., & Hirschfeld, A. 1974, ApJS, 28, 373
Sternberg, A., & Neufeld, D. A. 1999, ApJ, 516, 371
Teyssier, D., Hennebelle, P., & Pérault, M. 2002, A&A, 382, 624
Thi, W.-F., van Dishoeck, E. F., Blake, G. A., van Zadelhoff, G.-J., & Hogerheijde, M. R. 1999, ApJ, 521, L63
Valentijn, E. A., & van der Werf, P. P. 1999, ApJ, 522, L29
Valentijn, E. A., Feuchtgruber, H., Kester, D. J. M., et al. 1996, A&A, 315, L60
Valentijn, E. A., & Thi, W. F. 2000 (VT00), Experimental Astronomy, 10, 215
Weaver, H., & Williams, D. R. W. 1973, A&AS, 8, 1
Wolfire, M. G., McKee, C. F., Hollenbach, D., & Tielens, A. G. G. M. 2003, ApJ, 587, 278

# Online Material

## Appendix: Detecting faint lines in SWS data

The line fluxes given in Sect. 2.3 are amongst the faintest ever detected by the SWS instrument (see also Valentijn & van der Werf 2000; and Thi et al. 1999). Beside standard SWS-IA reduction routines, in-house tools were used to reach the ultimate sensitivity of the SWS detectors. We describe below the reduction procedure employed here and the new tools implemented.

We first corrected all of our integration ramps for the reset pulse shape. Indeed, the signal of the SWS detectors is the slope of 2 seconds voltage ramps read out at 24 Hz (48 points per ramp). After each ramp, a reset voltage pulse is applied which produces strong oscillations which partially propagate into the next ramp. These oscillations, sometimes seen throughout a whole ramp, are called the *pulse shape*. In addition, each detector is coupled to a high-pass filter and the voltage ramp is curved as in a loading capacitor with a RC time constant. It can be shown that the output voltage is the sum of the pulse shape, the RC curvature term and of the linear ramp sought for (Leech et al. 2000). Thus, to obtain the real slope, each ramp must be *linearized*, i.e., the reset pulse shape and the RC curvature terms must be subtracted. Pulse shapes and RC time constants must be found for each detector; moreover, they are known to vary from one orbit to the other because of the processing induced by the energetic particles present in space (Valentijn & Thi 2000, hereafter VT00). In the standard pipeline, the RC time constants derived from ground-level tests are used and no pulse shape correction is applied. To obtain the best signal estimate and meaningful slope error or STDEV[2], we use the self-calibration method of VT00. It determines first the mean pulse shape and then finds the RC time constants which minimize the STDEV of our observations: this was done with the `derive_pulse_shape` routine of SWS-IA. This method implicitly assumes the ideal case where the RC curvature and the pulse shape can be treated independently of each other and of the signal (the linear term in the ramp). As the RC curvature and the pulse shape are additive terms to the ramp, they do not, in principle, depend on the signal: we therefore used only the dark current measurements to estimate the pulse shape and RC time constants. Minor deviations from the ground-level test values of the RC time constants were found. Conversely, the pulse shape correction greatly improved the ramp linearization. The signal was then derived using the new pulse shapes and RC time constants in the standard pipeline procedure. To monitor any alteration of the absolute flux scale introduced by our pulse shape correction, we ran reductions without this step: no significant changes were found for the absolute calibration of the continuum.

To reach the ultimate sensitivity of the SWS, it is essential to remove the glitches (cosmic ray hits on detectors). We identify glitches on two basis, namely, *method A*: a detector hit by a glitch has a large STDEV and *method B*: after flux calibration, a glitch lies out the coherent features found in the robust mean of the redundant SWS signal. To detect glitches with method *A*, we inspect the slope residues *before* the flux calibration[3] and build STDEV histograms for each detector. As expected, each histogram looks like a Gaussian to which a tail at high STDEV values has been added: the contribution from glitches. To suppress this glitch tail, we first estimate the full width at half maximum (*FWHM*) of the histogram towards the low STDEV side (i.e., unaffected by the glitches). We then reject all data points with STDEV values lying out the value *max*(STDEV histogram) + *FWHM* (or the absolute 0.6 $\mu$V/s limit, see VT00). In addition, a significant reduction of the rms of the high-frequency (HF) signal was obtained by also discarding the data point just after a glitch[4]. Method *A* is very sensitive and can detect weak-level glitches. Indeed, it uses the statistical information contained in the 48 read-outs per ramp (method *B* does not); and it is also independent of the signal-to-noise ratio of the data (whereas method *B* is based on it). Conversely, glitch recognition with method *B* relies on the coherence (or the reproducibility) of the signal seen in the 24 *elementary scans*[5] of the SWS: thus, the two deglitching methods are complementary.

Glitches were removed with method *A* just after deriving the slopes of integration ramps: in this step a reduction of 40% on the signal rms noise was achieved at the cost of discarding 45% of the data points. Next comes the dark current subtraction operation. In SWS-AOT2 data, dark current is measured 10 times before and after a DOWN/UP scan. After rejection of bad dark points with method *A*, we take the robust mean of the 10 dark points before and after the DOWN/UP scan and perform a linear interpolation between these two points. This dark current estimate is then subtracted from all data points. We also tried to subtract a higher degree polynomial dark current (VT00) but the results were poorer. The flux calibration is then done in two steps: (i) the signal is divided by the Relative Spectral Response Function (RSRF) of each detector; and (ii) the absolute flux scale at key wavelengths is established (Schaeidt et al. 1996). The RSRF of the spectral bands 2 (7 to 12 $\mu$m) and especially 3 (12 to 16.5 $\mu$m) of the SWS are affected by interference fringes. In flight, the RSRF fringes (amplitude, phase) may depend on the extent of the source and its position in the SWS aperture. We obtained best results (i.e., in the agreement of the UP and DOWN scan) while using the `resp_inter` routine of SWS-IA. `resp_inter` shifts the RSRF fringes and modifies their amplitude in order to find the maximum of correlation with the signal (when shifts larger than two resolution elements were found, we did not apply them). Once the maximum is found, the RSRF division is performed with the best values of the fringes phase and amplitude. We used RSRF calibration files CAL25 version 040.

We now have 24 elementary scans of the same spectral region. To get down to a Gaussian noise distribution,

[2] The slope error is the root-mean-square (rms) noise of the voltage ramp after subtraction of the reset pulse shape, the RC curvature term and the linear fit, divided by the ramp duration.

[3] During flux calibration, the signal is divided by the instrumental response: hence, the STDEVs are altered and have a more complicated statistical distribution which depends on the flux value.

[4] After receiving a glitch, a detector may recover in a time longer than the ramp duration (2 s) so that the next ramp is also affected.

[5] We call elementary scan, the signal seen by a single detector during a given scan direction (UP or DOWN). In an elemantary scan, there are 4 to 5 data points per resolution element.

we remove more outlyers with method *B*. A low frequency continuum (a sliding boxcar on 25 points, i.e., 5 resolution elements) is first subtracted from each elementary scan to create high-frequency (HF) elementary scans. The HF elementary scans which now contain unresolved lines, glitches and noise, are combined by wavelength. The combined HF spectrum has 110 points per resolution element; we smooth it with a 10-points sliding boxcar to improve the signal-to-noise ratio while retaining enough spectral sampling to detect true HF features in the spectrum such as unresolved lines. We then subtract (after rebinning) this mean HF spectrum from each HF elementary scan, leaving residual elementary scans which in principle only contain noise and glitches. Glitches are finally removed from each residual elementary scan by 2-$\sigma$ clipping (about 10% of the data points were identified as glitches while gains of up to 40% were recorded on the rms noise of the HF signal).

We then correct the signal for correlated noise, i.e., weak level blips appearing in all detectors at the same time (e.g., due to electrical noise, see VT00). Correlated noise can produce artefact features in the data. As in the method *B* described above, we first generate HF elementary scans and combine them in the time domain. To correct for correlated noise, we then subtract the mean HF signal (after 2-$\sigma$ rejection) from each HF elementary scan at each reset point. The individual low frequency continuum is subsequently restored into each corrected HF elementary scan. The rms noise of the HF signal is reduced by about 10% in this operation.

Low-frequency variations in the detector responsivity due to in-orbit conditions must also be corrected: this is the flatfield operation which we performed with the `sws_flatfield` routine of SWS-IA. Continuum levels of a given line profile scan have been offset to a reference level. The offset values have been derived from first order fits to each elementary scan. The flatfield reference of a given line profile scan was the DOWN data. As our 200 s line profile scans are all repeated several times, we use the robust mean of all DOWN scans as the reference for flatfield.

Since the flatfielding has brought all elementary scans to the same low-frequency continuum level, we deglitch again (method *B*) to sweep off outlyers that were not distinguishable before. This time, the full mean signal is used (not only its HF part) to identify the statistically significant features. As above, the same sigma-clipping is applied to the difference between each elementary scan and the full mean spectrum. Less than 5% of points were recognized as glitches for a 20% decrease of the signal rms noise.

Finally, the signal is averaged *versus* wavelength (in micrometers) with a boxcar whose width corresponds to the instrumental resolution. Since at this stage most of the glitches have been removed, all the data carries a statistically significant information (i.e., within the 3-sigma limit): we therefore took a weighted mean of all points falling in a resolution element. The weight of each data point was estimated as follows. First, the robust mean of the signal is computed with a boxcar over each resolution element. This mean signal is then rebinned to each elementary scan and subtracted from it: the residual now only contains Gaussian noise and we estimate its standard deviation, $\sigma_r$. Each data point of the elementary scan is then given a weight equal to $1/\sigma_r^2$.